

# The Detection of ${}^3\text{He}^+$ in a Planetary Nebula Using the VLA

Dana S. Balser<sup>1</sup>, W. M. Goss<sup>2</sup>, T. M. Bania<sup>3</sup> & Robert T. Rood<sup>4</sup>

## ABSTRACT

We used the VLA to search for  ${}^3\text{He}^+$  emission from two Galactic planetary nebulae (PNe): NGC 6572 and J 320. Standard stellar models predict that the  ${}^3\text{He}/\text{H}$  abundance ratios for PNe should be 1–2 orders of magnitude higher than the primordial value ( ${}^3\text{He}/\text{H} \sim 10^{-5}$  by number) determined from Galactic H II region abundances and confirmed by WMAP cosmic microwave background results. Chemical evolution models suggest that fewer than 5% of all PNe enrich the interstellar medium (ISM) with  ${}^3\text{He}$  at the level of standard stellar models. Our target PNe are therefore anomalous in that they were selected from a sample deliberately biased to contain objects with properties that maximized the likelihood of a  ${}^3\text{He}$  detection by the VLA. We have detected the 8.665 GHz hyperfine  ${}^3\text{He}^+$  transition in J 320 at the  $4\sigma$  level. The  ${}^3\text{He}/\text{H}$  abundance ratio is  $1.9 \times 10^{-3}$  with roughly a factor of two uncertainty. For NGC 6572 we find an upper limit of  ${}^3\text{He}/\text{H} \lesssim 10^{-3}$ . This detection of  ${}^3\text{He}$  in J 320 makes it the second PN known to have an anomalously high  ${}^3\text{He}$  abundance confirming that at least some low-mass stars produce significant amounts of  ${}^3\text{He}$  that survives to the PN stage and enriches the ISM.

*Subject headings:* ISM: abundances — planetary nebulae: general — radio lines: ISM

## 1. Introduction

The light elements,  ${}^2\text{H}$  (D),  ${}^3\text{He}$ ,  ${}^4\text{He}$  and  ${}^7\text{Li}$ , are expected to be produced during the era of primordial nucleosynthesis and then further processed by stars over many generations

---

<sup>1</sup>National Radio Astronomy Observatory, P.O. Box 2, Green Bank WV 24944, USA.

<sup>2</sup>National Radio Astronomy Observatory, Socorro, NM 87801, USA.

<sup>3</sup>Institute for Astrophysical Research, 725 Commonwealth Avenue, Boston University, Boston MA 02215, USA.

<sup>4</sup>Astronomy Department, University of Virginia, P.O.Box 3818, Charlottesville VA 22903-0818, USA.

(Reeves 1974; Boesgaard & Steigman 1985). Observations of the light elements can in principle be used to constrain models of stellar and Galactic evolution and cosmology. For each light element the quantity of interest is the abundance ratio relative to hydrogen (e.g.,  ${}^3\text{He}/\text{H}$ ). In some cases converting the observables into an abundance ratio can be as difficult as making the observations.

For many years the light elements have been used to constrain standard Big Bang nucleosynthesis (SBBN) models (Copi et al. 1995). SBBN contains only one free parameter, the baryon-to-photon ratio,  $\eta_b$ . Observations of optical recombination lines of  ${}^4\text{He}$  in metal poor galaxies were first used to probe SBBN (Peimbert & Torres-Peimbert 1974). Observations of the resonance line of  ${}^7\text{Li}$  in metal poor Halo stars revealed a constant  ${}^7\text{Li}/\text{H}$  abundance ratio, called the “Spite Plateau”, that was interpreted as the primordial abundance and used to determine values of  $\eta_b$  (Spite & Spite 1982). The advent of large aperture, optical telescopes provided the sensitivity to detect the Lyman-series lines of D in metal poor QSO absorption systems (Tytler et al. 1996). More recently the  ${}^3\text{He}^+$  hyperfine transition was used to estimate  $\eta_b$  by measuring  ${}^3\text{He}/\text{H}$  in H II regions throughout the Galaxy. A “ ${}^3\text{He}$  Plateau” was discovered and from it a primordial abundance inferred (Bania et al. 2002, and shown in Figure 1). Since the primordial D/H abundance ratio is more sensitive to  $\eta_b$ , and the processing of D in stars is thought to be understood, it became the baryometer of choice by many investigators (Schramm & Turner 1998, for example). Nonetheless, *all* the light element abundances should agree with SBBN within the uncertainties.

Observations of the cosmic microwave background (CMB) provide an independent method of determining  $\eta_b$ . CMB anisotropy measurements made with the Wilkinson Microwave Anisotropy Probe (WMAP) were used by Spergel et al. (2003) to derive the primordial baryon-to-photon ratio. Adopting the CMB results for  $\eta_b$  gives the primordial light element abundances (Romano et al. 2003; Cyburt et al. 2003; Coc et al. 2004; Izotov & Thuan 2004; Steigman 2005). The D and  ${}^3\text{He}$  abundances are in good agreement with those derived from the WMAP observations. Depending on the adopted uncertainties the measured  ${}^4\text{He}$  abundance is either in agreement with CMB data or slightly lower than expected (Peimbert et al. 2003; Olive & Skillman 2004). The  ${}^7\text{Li}$  abundance is significantly lower given the low dispersion of these measurements. A possible resolution of this result is that the  ${}^7\text{Li}$  abundances are depleted in metal poor Halo stars (Charbonnel & Primas 2005, and references within).

Figure 1 shows the  ${}^3\text{He}/\text{H}$  abundance ratio by number as a function of Galactocentric radius (Bania et al. 2002). The solid circles (and crosses) are  ${}^3\text{He}$  abundances for H II regions located throughout the Galaxy. Since H II regions are very young, they measure the  ${}^3\text{He}/\text{H}$  abundance ratio at the present time. Not plotted are the  ${}^3\text{He}/\text{H}$  abundances for

protosolar material and the local ISM derived from the *Galileo Probe* (Mahaffy et al. 1998) and *Ulysses* (Gloeckler & Geiss 1998), respectively, that are in accord with the H II region  $^3\text{He}$  abundances. The solid triangle is the  $^3\text{He}$  abundance for the planetary nebula NGC 3242. Early stellar and Galactic evolution models predicted that solar type stars would produce and eventually expel into the ISM prodigious amounts of  $^3\text{He}$ , creating an easily measurable abundance gradient with Galactocentric radius or metallicity (Rood et al. 1976). The high  $^3\text{He}$  abundance in NGC 3242 was consistent with these early models but inconsistent with the H II region  $^3\text{He}$  abundances, stimulating a new generation of models.

In standard stellar models  $^3\text{He}$  is produced on the main sequence outside the main nuclear burning regions where p-p burning terminates in  $^3\text{He}$ . Longer lived low mass stars produce more  $^3\text{He}$ . This  $^3\text{He}$  is mixed into the convective envelope at the first dredge up on the lower red giant branch. Once in the envelope the  $^3\text{He}$  survives, so any stellar winds and the final PN should be substantially enriched in  $^3\text{He}$ .

Standard stellar models include only mixing produced by thermal convection. Observations have long indicated that *extra mixing* processes must be taking place, e.g., overshooting beyond convective radiative boundaries or rotationally induced turbulence (Zahn 1992). Charbonnel et al. (1998) argued that this rotationally induced extra-mixing occurs in low mass stars above the luminosity function bump produced when the hydrogen burning shell crosses the chemical discontinuity left by the retreating convective envelope early in the red giant branch phase. This hypothesis was supported by observed increases in the  $^{13}\text{C}$  abundance above the luminosity function bump. The same mixing that would increase the  $^{13}\text{C}$  abundance would bring the  $^3\text{He}$  down to values comparable to the primordial value. Further extra-mixing could take place on the second ascent asymptotic giant branch. In stars which have undergone extra mixing the material expelled into the ISM during the PN stage is therefore not enriched in  $^3\text{He}$  as originally thought. Charbonnel & do Nascimento (1998) predict that 96% of all low-mass stars will undergo this mixing process. The expected  $^3\text{He}$  yields coupled with Galactic evolution models (Tosi 2000; Chiappini et al. 2002; Galli 2005) are consistent with the “ $^3\text{He}$  Plateau” shown in Figure 1 and described by Bania et al. (2002).

The horizontal grey band in Figure 1 is the  $^3\text{He}/\text{H}$  primordial abundance ratio predicted by SBBN calculations (Burles et al. 2001) using the WMAP  $\eta_b$  value. The CMB abundance lies at the lower envelope of the  $^3\text{He}/\text{H}$  abundances. This and the absence of an observable negative gradient in the  $^3\text{He}$  abundances with galactocentric radius led Bania et al. (2002) to argue that the stellar contribution to  $^3\text{He}$  is positive definite but very small. The scatter in the H II region abundances could be real (e.g., azimuthal abundance fluctuations). But this scatter could also be measurement error (e.g., the ionization correction could be un-

derestimated for some H II regions). The scatter presumably obscures a yet to be observed gradient. Given this, a limit on BBNS production can be determined from the best determined abundance in the outer Galaxy. The rightmost solid point in Figure 1, the H II region S209, fits this requirement, and Bania et al. (2002) took the S209 abundance as their best estimate of the primordial abundance. This value is almost identical to the WMAP value.

There are two observational paths to improving our understanding of the evolution of  ${}^3\text{He}$ . The first is to reduce the scatter in the H II region abundances by observing a sample chosen because of their simple physical structure and optimum location in the Galaxy. The second is to observe the stellar sources of  ${}^3\text{He}$  and directly measure the  ${}^3\text{He}/\text{H}$  abundance in PNe.

Previous observations of six PNe were made using the Max Planck Institut für Radioastronomie 100 m telescope (Balser et al. 1997). The PN sample was chosen based on criteria that would maximize detection, including diagnostics that indicated less mixing.  ${}^3\text{He}^+$  was only detected in NGC 3242, shown as the solid triangle in Figure 1. It therefore appears that in at least one object significant amounts of  ${}^3\text{He}$  in a low-mass star survives until the PN phase, and that PN and its earlier stellar winds have enriched  ${}^3\text{He}$  in the ISM. We now seek to understand why some stars produce  ${}^3\text{He}$  and others do not.

Observations of  ${}^3\text{He}^+$  in PNe are challenging because of the weak intensity of the  ${}^3\text{He}^+$  emission line coupled with their small angular size. We are increasing the size of our PN sample using the Very Large Array (VLA), the 100 m Green Bank Telescope (GBT), and the 305 m Arecibo telescope. Our target sample is purposely biased to maximize detections. Our target selection criteria have evolved with time. Currently they are:

- Any mixing in the progenitor star beyond that included in standard stellar models is likely to destroy  ${}^3\text{He}$ . Indications of mixing include: high  ${}^{13}\text{C}/{}^{12}\text{C}$ , N/O, and  ${}^4\text{He}/\text{H}$  abundances. To be included as one of our targets a PN must have a  ${}^4\text{He}/\text{H}$  abundance ratio  $< 0.125$  by number and  $[\text{N}/\text{O}] < -0.3$  with a value  $< -0.6$  considered even better. Unfortunately the  ${}^{13}\text{C}/{}^{12}\text{C}$  abundance ratio is known for only a small sample of PNe (Clegg et al. 1997; Palla et al. 2000, 2002; Balser et al. 2002).
- The  ${}^3\text{He}$  abundance in the progenitor grows as main sequence lifetime increases, hence PNe from older stellar populations are more promising candidates. The Peimbert Class (Peimbert 1978; Faúndez-Abans & Maciel 1987) gives an estimate of the progenitor age (as well as abundance criteria similar to ours). Our targets are chosen from classes IIb, III, and IV.
- Since we observe  ${}^3\text{He}^+$ , our target PNe must have excitations such that most of the He is singly ionized.

Here we discuss  $^3\text{He}^+$  VLA observations of two PNe: NGC 6572 and J 320. Both objects are expected to have high  $^3\text{He}/\text{H}$  abundance ratios; they were selected using criteria similar to those above. In addition, the angular sizes of these PNe are well matched to the VLA synthesized beam at 8.7 GHz.

## 2. Observations

Table 1 summarizes the VLA<sup>1</sup> D-array configuration observations. NGC 6572 was observed on five different days. The correlator spectrometer was setup to observe the  $^3\text{He}^+$  hyperfine transition at two orthogonal polarizations at a rest frequency of 8665.65 MHz. The data were Hanning smoothed on-line. During part of the first day the H 91 $\alpha$  transition was observed at a rest frequency of 8584.81 MHz. J 320 was observed on seven different days. The correlator was setup to observe the  $^3\text{He}^+$  and H 91 $\alpha$  transitions simultaneously at two orthogonal polarizations each. The data were Hanning smoothed off-line.

The data were edited and calibrated using the Astronomical Image Processing System (AIPS). The calibrator 3C 286 was used to calibrate the intensity scale. Because the  $^3\text{He}^+$  emission line intensity was expected to be weak the bandpass had to be carefully calibrated. The spectral baselines are typically much flatter for interferometers than single-dish telescopes since any telescope dependent effect will be removed when the data from different antennas are cross correlated. But at the sensitivity levels required for our observations the VLA bandpass is not stable with time; amplitude variations as large as 1% have been measured with an approximate width of 3 MHz.<sup>2</sup> These baseline ripples are caused by reflections in the waveguides and move across the bandpass at about 0.4 MHz per hour. We therefore observed a bandpass calibration source approximately every 15 minutes for a duration of about 5 minutes. A bandpass model was calculated by interpolating the bandpass solutions over time. We are confident that we have removed most of this structure since the measured spectral rms noise is consistent with the expected thermal noise.

The continuum intensities of NGC 6572 and J 320 were sufficient to perform the standard self-calibration technique. We applied the self-calibration algorithm to each day’s observations after the standard phase and bandpass calibration. This procedure typically improved the signal-to-noise ratio by a factor of five in the continuum. The task DBCON was used to average the data. The self-calibration technique was applied to the final average. The task

---

<sup>1</sup>The National Radio Astronomy Observatory is a facility of the National Science Foundation operated under cooperative agreement by Associated Universities, Inc.

<sup>2</sup>See “A Guide for Spectral Line Observers” at <http://www.vla.nrao.edu/astro/guides/sline/current/>

UVLSF was used to subtract the continuum emission in the  $(u, v)$ -plane using the line-free channels. This fits a linear baseline to the specified channels in the real and imaginary parts of the visibilities. Continuum and line images were produced using the CLEAN algorithm. Table 1 lists the rms noise in these images. The continuum images are completely limited by the finite dynamic range of the strong continuum and thus are not limited by thermal fluctuations. The line data, after subtraction of the continuum, are limited by thermal noise. Thus the continuum rms values are larger than the line data.

### 3. Observational Results

The continuum images of NGC 6572 and J 320 are shown in Figures 2 and 3, respectively. The continuum emission is well modeled by a Gaussian function. The task JMFIT was used to fit a single-component, two-dimensional Gaussian model to the continuum image for each PN. Table 2 summarizes the results. Listed are the source name, the B1950 equatorial coordinates of the peak radio emission, the peak flux density, the integrated flux density, and the angular size.

We analyzed the H 91 $\alpha$  and  $^3\text{He}^+$  spectral line data cubes using four different methods: (1) the ISPEC task was used to produce spectra toward the continuum peak emission within a single resolution element; (2) averages over different spatial areas were made in order to increase the signal-to-noise ratio; (3) the images were convolved with Gaussian functions that had half-power beam-widths (HPBW's) larger than the synthesized beam; and (4) the task IRING was used to compute averages over concentric annuli to produce a cumulative flux density versus radius relation. This latter method averages over both position and velocity.

We detected H 91 $\alpha$  line emission in both PN; only J 320 has  $^3\text{He}^+$  emission. Spectra are shown in Figures 4 and 5 for NGC 6572 and in Figures 6 and 7 for J 320. The solid line histograms are the data and the dashed lines are models described in §4. The additional spectra shown for J 320 were made by convolving the H 91 $\alpha$  data cube with a HPBW of 20'' (Figure 6) and the  $^3\text{He}^+$  data cube with HPBW's of 20, 30, and 40'' (Figure 7). Comparing the  $^3\text{He}^+$  line intensity to the noise level in the line free region in Figure 7 shows that the detection has a signal to noise ratio of  $S/N \sim 4$ . Figure 8 plots the cumulative  $^3\text{He}^+$  flux density from the  $^3\text{He}^+$  channels (12–22) versus radius for J 320. The  $^3\text{He}^+$  flux density gradually increases until a radius of 15–20''. For larger radii the flux drops because of missing short spacing data. In the configuration used for these observations the VLA has no sensitivity to  $^3\text{He}^+$  emission with radii larger than about 30''. The plot also shows the cumulative flux density for the channels not containing the line emission (6–11 & 23–26). A comparison of the line and line-free results gives a  $S/N$  of  $\sim 9$  for the  $^3\text{He}^+$  detection. This

value is larger than that obtained from the spectra because the  ${}^3\text{He}^+$  emission is averaged over both space and frequency. The detected continuum and recombination line emission are both confined to a smaller area within a radius of 5–10". Apparently much of the  ${}^3\text{He}^+$  emission from J 320 emanates from a large, low density halo. The model shown in Figure 8 has a 35" halo (see § 4.2). This halo model fits the data well except for larger radii where it is not affected by the missing short baselines.

#### 4. The ${}^3\text{He}$ Abundance

Estimates for the  ${}^3\text{He}/\text{H}$  abundance ratios in the PNe were made by numerical modeling. We used the radiative transfer code NEBULA to calculate synthetic spectra of the radio continuum, radio recombination line, and  ${}^3\text{He}^+$  line emission from a model nebula (Balsler et al. 1999a). The model is comprised solely of ionized hydrogen and helium gas. A density and ionization structure is specified within a three-dimensional Cartesian coordinate system. For each numerical cell the following physical properties are specified: electron temperature ( $T_e$ ), electron density ( $n_e$ ), and helium ionization ( ${}^4\text{He}^+/\text{H}^+$ ,  ${}^4\text{He}^{++}/\text{H}^+$ ,  ${}^3\text{He}^+/\text{H}^+$ ). The modeled nebula consists of homogeneous concentric shells which have a radial expansion velocity (Balsler et al. 1997, 1999b). The line profile is therefore broadened by three components: thermal, microturbulent, and large-scale expansion. The thermal motions are determined from the electron temperature, whereas the microturbulent motions, by definition smaller than the numerical cell, are set by a single free parameter that is constrained by the observed linewidths. The  ${}^3\text{He}^+$  and recombination lines are assumed to be in LTE. Non-LTE effects and pressure broadening from electron impacts are negligible for these PN models. Synthetic spectra are generated by calculating the radiative transfer for the line and continuum emission as a function of frequency from the back to the front of the numerical grid. The NEBULA outputs are the two-dimensional continuum brightness distribution and spectral data cubes for  ${}^3\text{He}^+$  and the recombination lines. These model data are then convolved with a specified telescope beam so they can be compared directly with observations.

We use an iterative procedure to derive an estimate for the  ${}^3\text{He}/\text{H}$  abundance. First the physical properties of a source are constrained by the continuum and recombination line emission as well as data from the literature. A fiducial  ${}^3\text{He}/\text{H}$  abundance is then chosen and synthetic spectra are calculated with NEBULA. The  ${}^3\text{He}/\text{H}$  abundance is iterated until the model spectra match the observations. A grid of models is used to assess the uncertainty in the derived  ${}^3\text{He}/\text{H}$  abundance.

The planetary nebulae properties used as input for NEBULA are summarized in Table 3. The PNe distance, expansion velocity, and helium ionization structure are taken from the

literature (see §4.1–4.2). The VLA data are used to model the PNe as single, homogeneous, spheres (Balsler et al. 1995, 1999a). From these models we determine the spherical angular size, electron temperature, and electron density. Below we discuss each PN separately.

#### 4.1. NGC 6572

NGC 6572, discovered by Struve in 1825, is a well studied planetary nebula (Acker et al. 1992). Unlike most PNe the distance to NGC 6572 has been accurately measured by combining the angular expansion rate, determined from high spatial resolution radio continuum images at two or more epochs, with the Doppler expansion velocity (Masson 1986). We adopt a distance to NGC 6572 of 1.2 kpc (Kawamura & Masson 1996). The expansion velocity is directly measured from spectral line data that resolves the PN shell (Masson 1989; Acker et al. 1992). The helium ionization properties are taken from Cahn et al. (1992).

The VLA data were used to model a single, homogeneous sphere with an angular size of  $7''.9$ . Although NGC 6572 is just resolved by our VLA data this size is consistent with other estimates (Acker et al. 1992). NGC 6572 has been imaged at higher resolution in the radio (Masson 1989), near infrared (Hora et al. 1990), and optical (Miranda et al. 1999). Morphologically, NGC 6572 has a double-lobed, elliptical structure with a central minimum. We assume an inner shell size of  $2''$ . The electron temperature and density are found to be 10,300 K and  $22,000 \text{ cm}^{-3}$ , respectively. Various values for  $T_e$  and  $n_e$  can be found in the literature. These values depend on the spectral lines employed, the method used to determine these physical parameters, and the volume within the nebula sampled since real temperature and density fluctuations are present (Mathis et al. 1998). For example, electron temperatures determined from optical forbidden line ratios are weighted toward higher temperature regions whereas radio recombination line-to-continuum ratios are weighted toward lower temperature regions (Mansfield 1969). Nevertheless, our estimates are in good agreement with Zhang et al. (2004), who use the optical hydrogen recombination spectrum to determine  $T_e$  and  $n_e$ .

The model results are shown as dashed curves in Figures 4 and 5 for the H 91 $\alpha$  and  $^3\text{He}^+$  lines, respectively. The H 91 $\alpha$  model profile is a good fit to the observations. The data are consistent with an upper limit for the  $^3\text{He}/\text{H}$  abundance ratio of  $\lesssim 10^{-3}$ .



## 4.2. J 320

Discovered in 1913 (Jonckheere 1913), J 320 has a radio continuum flux density about 50 times weaker than NGC 6572; thus it is not as well studied. The morphology and kinematics of J 320 have recently been investigated using long slit spectroscopy with the Anglo-Australian Telescope (AAT) and  $H\alpha$  images with the Hubble Space Telescope (HST) (Harman et al. 2004). The central nebula consists of two (possibly three) bipolar lobes expanding at  $\sim 46 \text{ km sec}^{-1}$  with different orientations. The morphology is thus better classified as a poly-polar PN. Surrounding the central nebula are high speed knots that may not have played a significant role in forming the central nebula.

The distance estimates to J 320 vary from 2 to 6 kpc using different methods (Harman et al. 2004, and references within). Here we adopt a distance of 5 kpc. The helium ionization properties are taken from Cahn et al. (1992). The VLA radio continuum and recombination line data are used to determine the angular size, electron temperature, and electron density. The angular size is  $7''.4$ , consistent with previous estimates (Acker et al. 1992; Tylenda et al. 2003). We assume an inner shell size of  $2''$ . The electron temperature and density are 7,500 K and  $1,500 \text{ cm}^{-3}$ , respectively; these values are lower than predicted by optical forbidden line ratios (Barker 1978; Cahn et al. 1992), as might be expected for a nebula with temperature and density fluctuations.

Because the  ${}^3\text{He}^+$  emission extends beyond the continuum emission, we infer that a low density halo exists for this PN (see Figure 8). Halo components are not uncommon for PNe but are difficult to detect in optical ( $H\alpha$  emission) or radio continuum (free-free emission) images since these tracers of ionized gas are proportional to the emission measure ( $\propto n_e^2$ ) and halo densities are typically low. The  ${}^3\text{He}^+$  emission, however, is sensitive to the total column density ( $\propto n_e$ ). Therefore it is plausible to detect the halo in  ${}^3\text{He}^+$  emission but not radio continuum emission. The same situation obtained for NGC 3242 (Balser et al. 1997, 1999b).

The  ${}^3\text{He}^+$  and radio continuum data together with NEBULA models were used to constrain some of the halo properties. To estimate the size of the halo we modeled the  ${}^3\text{He}^+$  emission using NEBULA for different halo sizes. Figure 9 plots the cumulative  ${}^3\text{He}^+$  flux density versus radius for the VLA data (solid curve) and for five different halo models (dashed curves). The electron density was assumed to be  $100 \text{ cm}^{-3}$  for all halo models and the cumulative  ${}^3\text{He}^+$  flux density was scaled to match the VLA data since we are only interested in the relative shape. Qualitatively a halo size of  $35''$  best fits the data. We set a limit for the halo electron density by calculating the continuum emission for different values of  $n_e$ . Figure 10 plots the cumulative continuum flux density versus radius for the VLA data (solid curve) and for five models (dashed curves) with different halo electron densities and

a halo size of  $35''$ . For halo densities between  $0 < n_e < 50 \text{ cm}^{-3}$  the predicted continuum emission is within 5% of the measured VLA continuum. The upper limit of  $n_e = 50 \text{ cm}^{-3}$  sets a lower limit to the predicted  ${}^3\text{He}/\text{H}$  abundance ratio. The expansion velocity of the halo is constrained by the  ${}^3\text{He}^+$  profile shape. Given the low signal-to-noise ratio of the  ${}^3\text{He}^+$  line and the complex morphology of J320, it is not clear how to interpret the double profile in Figure 7. In our models the Doppler thermal and microturbulent broadening together produce a Gaussian line shape. An expansion broadening, however, produces either a square-wave profile for an unresolved source or two separate peaks for an optically thin, resolved source. Nevertheless, in the context of our spherically symmetric expanding shell model we use the overall width of the  ${}^3\text{He}^+$  profile to estimate a halo expansion velocity of  $25 \text{ km sec}^{-1}$ .

Based on these constraints, we adopt a halo size of  $35''$ , an electron density of  $50 \text{ cm}^{-3}$ , and a uniform expansion velocity of  $25 \text{ km sec}^{-1}$ . Because we have no information about these physical properties in the halo, the electron temperature and ionization properties in the halo are assumed to be the same as the core values. Since the  ${}^3\text{He}/\text{H}$  abundance ratio is only weakly dependent on the electron temperature, having to use an assumed value is not a serious compromise. Furthermore, since the source of ionization is a hot central star all of the helium should be singly ionized.

The results are summarized in Figures 6–8. The solid lines are the data whereas the dashed curves are the model results assuming a  ${}^3\text{He}/\text{H}$  abundance of  $1.9 \times 10^{-3}$ . Overall the model fits the data reasonably well. The major uncertainties in determining the  ${}^3\text{He}/\text{H}$  abundance ratio in J320 are: (1) the measured line intensity; (2) the distance; (3) the halo electron density; and (4) the halo size. The  ${}^3\text{He}/\text{H}$  abundance ratio is proportional to  $T_L R_{\text{sun}}^{-1/2}$ , where  $T_L$  is the  ${}^3\text{He}^+$  line intensity and  $R_{\text{sun}}$  is the distance (Rood et al. 1984). Depending on how the signal-to-noise ratio is estimated, we detect  ${}^3\text{He}^+$  emission at a S/N of  $\sim 4$  or 9. Taking the more conservative value of 4, the uncertainty in the  ${}^3\text{He}/\text{H}$  abundance is  $\pm 0.5 \times 10^{-3}$ . An error of 1.5 kpc in the distance gives an error in the abundance of  $\pm 0.3 \times 10^{-3}$ . The VLA continuum image limits the halo electron density to less than  $50 \text{ cm}^{-3}$ . Smaller values of  $n_e$  are possible and will increase  ${}^3\text{He}/\text{H}$ . For example, a halo electron density of  $10 \text{ cm}^{-3}$  will increase  ${}^3\text{He}/\text{H}$  by 50%. The halo size is constrained by the distribution of  ${}^3\text{He}^+$  emission. But a larger halo may exist and not be detected by our observations. For example, if the halo size extends beyond about  $60''$  it would not be detected in  ${}^3\text{He}^+$  emission with the VLA. A larger halo will reduce our predicted value of  ${}^3\text{He}/\text{H}$ . For example, a halo size of  $100''$  will decrease the  ${}^3\text{He}/\text{H}$  abundance by 50%. None of these errors is likely to be normally distributed, so we cannot combine them in a meaningful way. Crudely, we estimate that the abundance error is roughly a factor of two.

## 5. Discussion

The most important result of this paper is that we have detected  ${}^3\text{He}^+$  in another planetary nebula, J 320, with a  ${}^3\text{He}/\text{H}$  abundance ratio roughly *two orders of magnitude larger* than the primordial value ( ${}^3\text{He}/\text{H} \sim 10^{-5}$  by number) determined from Galactic H II region abundances and confirmed by WMAP cosmic microwave background results. Merely detecting  ${}^3\text{He}^+$  in J 320 tells us that its stellar progenitor evolved in a manner well described by standard stellar models: it produced  ${}^3\text{He}$  during its main sequence lifetime; it did not undergo any extra-mixing; it subsequently expelled  ${}^3\text{He}$  enriched gas into the ISM. To be consistent with chemical evolution models, the existence of the  ${}^3\text{He}$  Plateau demands that the majority of PNe are not net producers of  ${}^3\text{He}$ . J 320 now joins NGC 3242 as only the second known example of those rare planetary nebulae which enrich the Galaxy in  ${}^3\text{He}$ .

Our long term goal is to identify some surrogate characteristics which allow us to determine what fraction of planetary nebulae enrich the ISM in  ${}^3\text{He}$  without having to measure  ${}^3\text{He}$  itself. Now that the sample of  ${}^3\text{He}$  PNe has a population of two we can begin this attempt. There are some intriguing similarities between NGC 3242 and J 320. They both satisfy our selection criteria: each has low He/H and [N/O] abundance which indicates little or no extra-mixing; each has most of its He in a singly ionized state; each originates from an old stellar population as indicated by its Peimbert Class (NGC 3242 is I Ib; J 320 is IV).

Superficially, all Peimbert Class I Ib, III & IV PNe should be good  ${}^3\text{He}$  targets. Class I Ib alone encompasses about 35% of all the known PNe (Quireza, private communication). In order to not over-produce  ${}^3\text{He}$ , there must be something in addition to either the Peimbert Class or our other selection criteria (or both) that determines which PNe have high  ${}^3\text{He}$  abundances. With the detection of  ${}^3\text{He}$  in J 320 we have a first hint as to what that parameter might be. Both detected PNe have low density halos which apparently produce the bulk of the  ${}^3\text{He}^+$  signal that we detect (Balsler et al. 1999b, and herein). Both have lineshapes that are consistent with optically thin expanding shells. Are low density halos required for high  ${}^3\text{He}$ , or do they simply make it easier to detect if present?

## 6. Conclusions

We detected  ${}^3\text{He}^+$  emission with the VLA in the planetary nebulae J 320. Using numerical models we derive a  ${}^3\text{He}/\text{H}$  abundance ratio by number of  $1.9 \times 10^{-3}$  with an uncertainty of roughly a factor of two. This value is two orders of magnitude higher than the typical  ${}^3\text{He}$  abundance found in Galactic H II regions. This detection makes J 320 the second planetary nebula known (together with NGC 3242) to have an anomalously high  ${}^3\text{He}$  abundance.

The research was supported by the National Science Foundation (AST 00-98047). We thank Cintia Quireza for discussions about PNe and providing her PNe database prior to publication. We thank the international light elements community for their friendship and support.

*Facilities:* VLA

## REFERENCES

- Acker, A., Ochsenbein, F., Stenholm, B., Tyllenda, R., Marcout, J., & Schohn, C. 1992, Strasbourg-ESO Catalogue of Galactic Planetary Nebulae (Garching: ESO)
- Balser, D. S., Bania, T. M., Rood, R. T., & Wilson, T. L. 1995, *ApJS*, 100, 371
- Balser, D. S., Bania, T. M., Rood, R. T., & Wilson, T. L. 1997, *ApJ*, 483, 320
- Balser, D. S., Bania, T. M., Rood, R. T., & Wilson, T. L. 1999a, *ApJ*, 510, 759
- Balser, D. S., McMullin, J. P., & Wilson, T. L. 2002, *ApJ*, 572, 326
- Balser, D. S., Rood, R. T., & Bania, T. M. 1999b, *ApJ*, 522, L73
- Bania, T. M., Rood, R. T., & Balser, D. S. 2002, *Nature*, 415, 54
- Barker, T. 1978, *ApJ*, 219, 914
- Boesgaard, A. M., & Steigman, G. 1985, *ARA&A*, 23, 319
- Burles, S., Nollett, K. M., Turner, M. S. 2001, *ApJ*, 552, L1
- Cahn, J. H., Kaler, J. B., & Stanghellini, L. 1992, *A&AS*, 94, 399
- Charbonnel, C., Brown, J. A., & Wallerstein, G. 1998, *A&A*, 332, 204
- Charbonnel, C. & do Nascimento Jr., J. D. 1998, 336, 915
- Charbonnel, C. & Primas, F. 2005, *A&A*, in press
- Chiappini, C., Renda, A., & Matteucci, F. 2002, *A&A*, 395, 789
- Clegg, R. E. S., Storey, P. J., Walsh, J. R., & Neale, L. 1997, *MNRAS*, 284, 348
- Coc, A., Vangioni-Flam, E., & Angulo, C. 2004, *ApJ*, 600, 544

- Copi, C. J., Schramm, D. N., & Turner, M. S. 1995, *Science*, 267, 192
- Cyburt, R. H., Fields, B. D., & Olive, K. A. 2003, *Phys. Lett.*, B567, 227
- Faúndez-Abans, M. & Maciel, W. J. 1987, *A&A*, 183, 324
- Galli, D. 2005, in the Proceedings of the ESO/Arcetri Workshop, Chemical Abundances and Mixing in Stars in the Milky Way and its Satellites, ed. L. Pasquini and S. Randich (Springer-Verlag: Berlin), in press
- Gloeckler, G. & Geiss, J. 1998, *Space Sci. Rev.*, 84, 275
- Harman, D. J., Bryce, M., López, J. A., Meaburn, J., & Holloway, A. J. 2004, *MNRAS*, 348, 1047
- Hora, J. L., Deutsch, L. K., Hoffmann, W. F., & Fazio, G. G. 1990, *ApJ*, 353, 549
- Izotov, Y. I., & Thuan, T. X. 2004, *ApJ*, 602, 200
- Jonckheere, R. 1916, *The Observatory*, 39, 134
- Kawamura, J., & Masson, C. 1996, *ApJ*, 461, 282
- Mahaffy, P. R., Donahue, T. M., Atreya, S. K., Owen, T. C., & Niemann, H. B. 1998, *Space Sci. Rev.*, 84, 251
- Mansfield, V. 1969, *Astrophysics and Space Science*, 3, 292
- Masson, C. R. 1986, *ApJ*, 302, L27
- Masson, C. R. 1989, *ApJ*, 346, 243
- Mathis, J. S., Torres-Peimbert, S., & Peimbert, M. 1998, *ApJ*, 495, 328
- Miranda, L. F., Vázquez, R., Corradi, R. L. M., Guerrero, M. A., López, J. A., & Torrelles, J. M. 1999, *ApJ*, 520, 714
- Olive, K. A., & Skillman, E. D. 2004, *ApJ*, 617, 29
- Palla, F., Bachiller, R., Stanghellini, L., Tosi, M., & Galli, D. 2000, *A&A*, 355, 69
- Palla, F., Galli, D., Marconi, A., Stanghellini, L., & Tosi, M. 2002, *ApJ*, 568, L57
- Peimbert, M. 1978, in *IAU Symp. 76, Planetary Nebulae*, ed. Y. Terzian (Dordrecht: D. Reidel), 215

- Peimbert, M., Peimbert, A., Luridiana, V., & Ruiz, M. T. 2003, in ASP Conf. Ser. 297, Star Formation Through Time, ed. E. Perez, R. M. Gonzalez Delgado & G. Tenorio-Tagle (San Francisco: ASP), 81
- Peimbert, M., & Torres-Peimbert, S. 1974, ApJ, 193, 327
- Readhead, A. C. S., et al. 2004, ApJ, 609, 498
- Reeves, H. 1974, ARA&A, 12, 437
- Romano, Tosi, Matteucci, & Chiappini 2003, MNRAS, 346, 295
- Rood, R. T., Bania, T. M., & Wilson, T. L. 1984, ApJ, 280, 629
- Rood, R. T., Steigman, G., & Tinsley, B. M. 1976, ApJ, 207, L57
- Rubin, R. H., Ferland, G. J., Chollet, E. E., & Horstmyer, R. 2004, ApJ, 605, 784
- Schramm, D. N., & Turner, M. S. 1998, Rev. Mod. Physics, 70, 303
- Spergel, D. N. et al. 2003, ApJS, 148, 175
- Spite, M., & Spite, F. 1982, Nature, 297, 483
- Steigman, G. 2005, in the Proceedings of the ESO/Arcetri Workshop, Chemical Abundances and Mixing in Stars in the Milky Way and its Satellites, ed. L. Pasquini and S. Randich (Springer-Verlag: Berlin), in press
- Tosi, M. 2000, The Light Elements and Their Evolution, IAU Symposium 198, eds. da Silva, L., Spite, M. & de Medeiros (ASP: San Francisco), 525
- Tylenda, R., Siódmiak, N., Górny, S. K., Corradi, R. L. M., Schwarz, H. E. 2003, A&A, 405, 627
- Tytler, D., Fan, X.-M., & Burles, S. 1996, Nature, 381, 207
- Zahn, J.-P. 1992, A&A, 265, 115
- Zhang, Y., Liu, X.-W., Wesson, R., Storey, P. J., Liu, Y., & Danziger, I. J. 2004, MNRAS, 351, 935

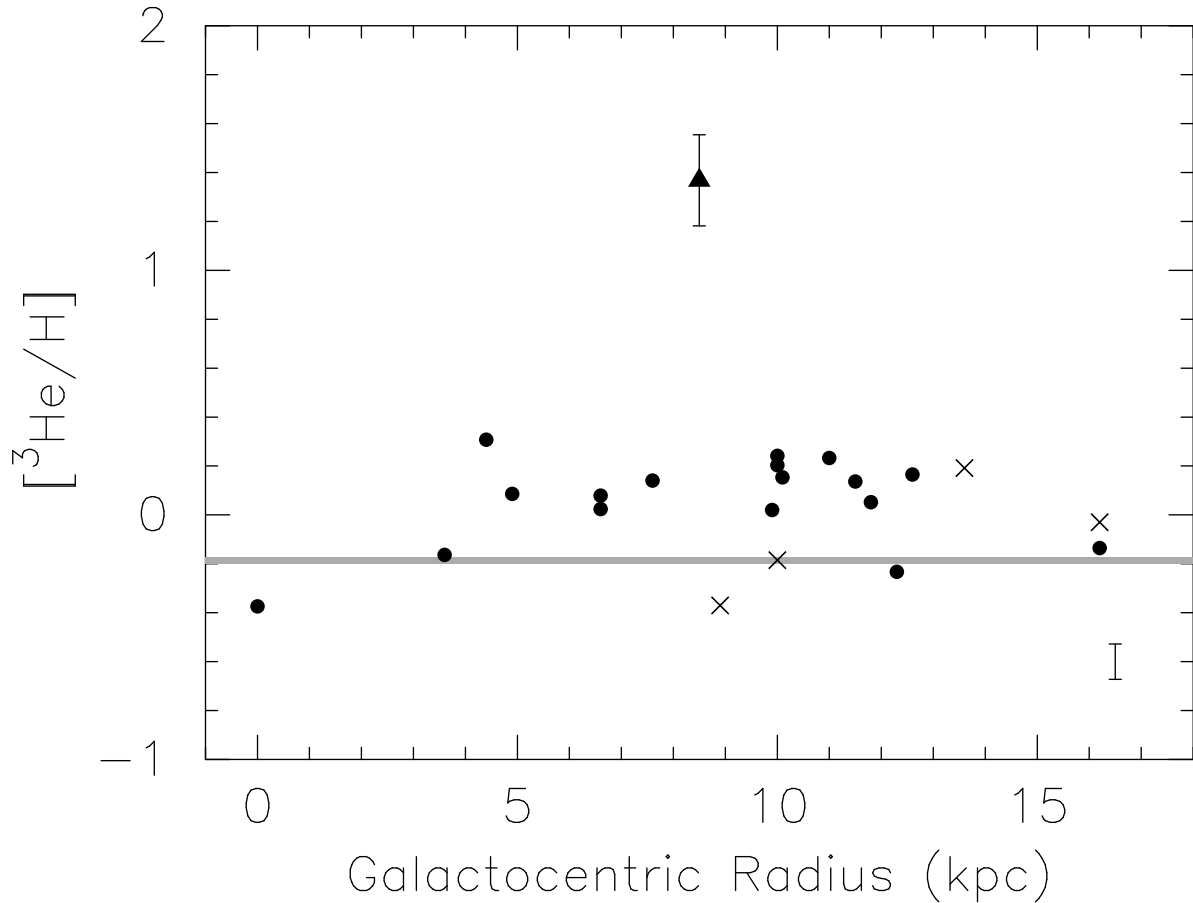


Fig. 1.—  ${}^3\text{He}/\text{H}$  abundance as a function of Galactocentric radius where  $[{}^3\text{He}/\text{H}] = \log({}^3\text{He}/\text{H}) - \log(1.5 \times 10^{-5})$ . The solid points and crosses are Galactic H II region  ${}^3\text{He}/\text{H}$  abundance ratios taken from Bania et al. (2002). The crosses correspond to H II regions where no ionization correction could be made and thus we may have underestimated the  ${}^3\text{He}/\text{H}$  abundances in these objects. The typical error is shown in the lower right hand corner. The triangle plots  $[{}^3\text{He}/\text{H}]$  for the planetary nebula NGC 3242 (Balsler et al. 1997). The thick solid line indicates the primordial  ${}^3\text{He}/\text{H}$  abundance predicted by Big Bang nucleosynthesis (Burles et al. 2001) assuming the WMAP baryon-to-photon ratio (Spergel et al. 2003).

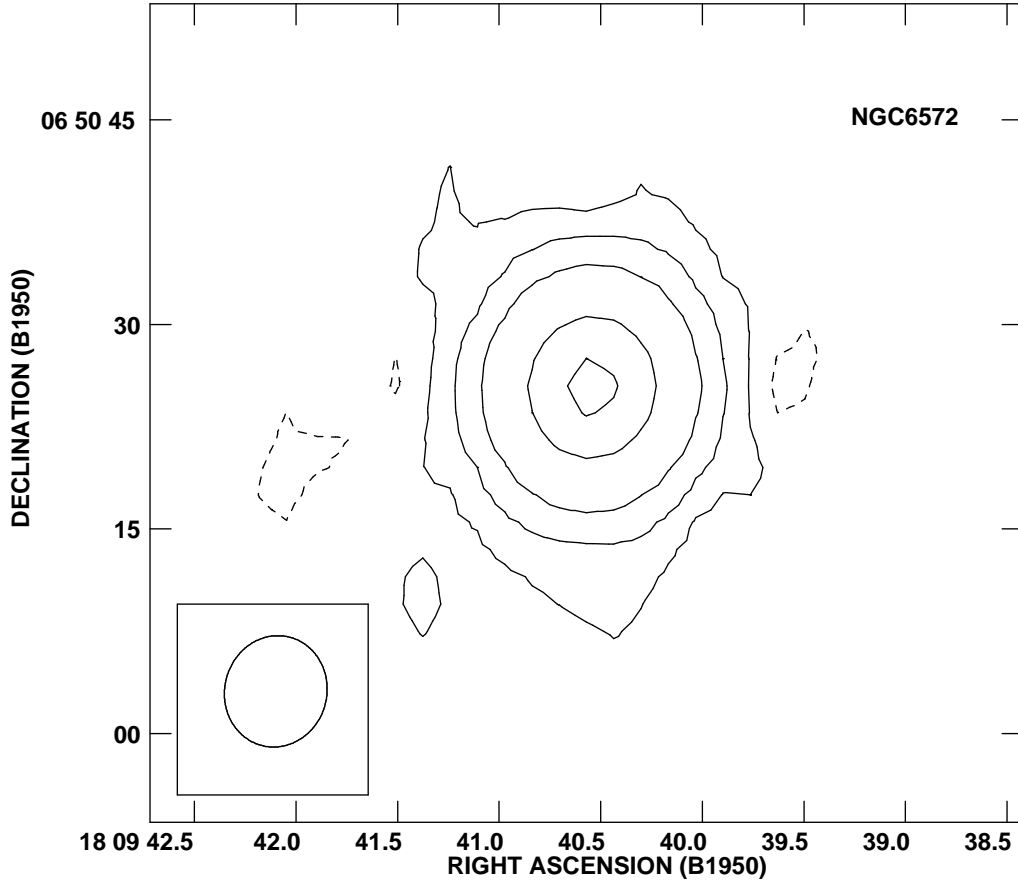


Fig. 2.— VLA continuum image of NGC 6572 at 8.7 GHz. The resolution,  $8''.20 \times 7''.49$  at a PA of  $-14^\circ$ , is indicated in the lower left-hand corner. The intensity scale is in units of  $\text{mJy beam}^{-1}$ . The contour levels are at  $-3$ ,  $3$ ,  $25$ ,  $100$ ,  $500$ , and  $1000$  times the  $3\sigma$  ( $0.834 \text{ mJy}$ ) noise level.



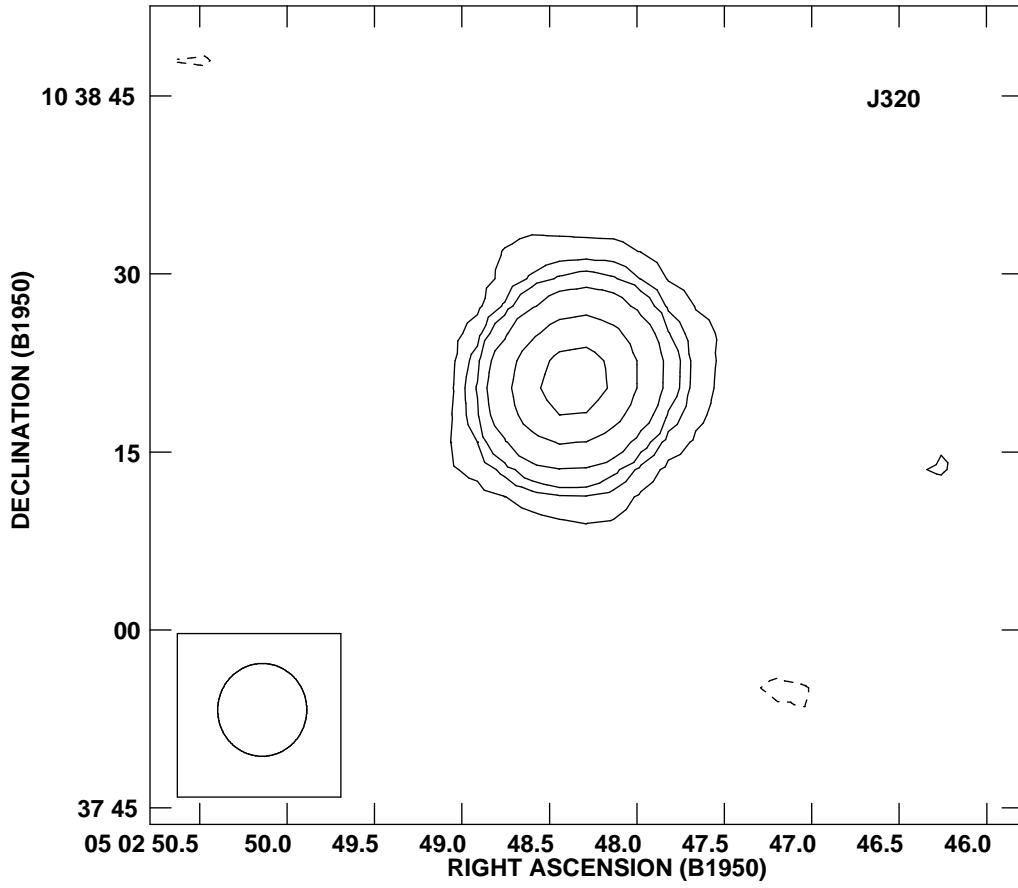


Fig. 3.— VLA continuum image of J320 at 8.7 GHz. The resolution,  $7''.82 \times 7''.51$  at a PA of  $-2^\circ$ , is indicated in the lower left-hand corner. The intensity scale is in units of  $\text{mJy beam}^{-1}$ . The contour levels are at  $-1, 1, 3, 5, 10, 25,$  and  $50$  times the  $3\sigma$  ( $0.264 \text{ mJy}$ ) noise level.

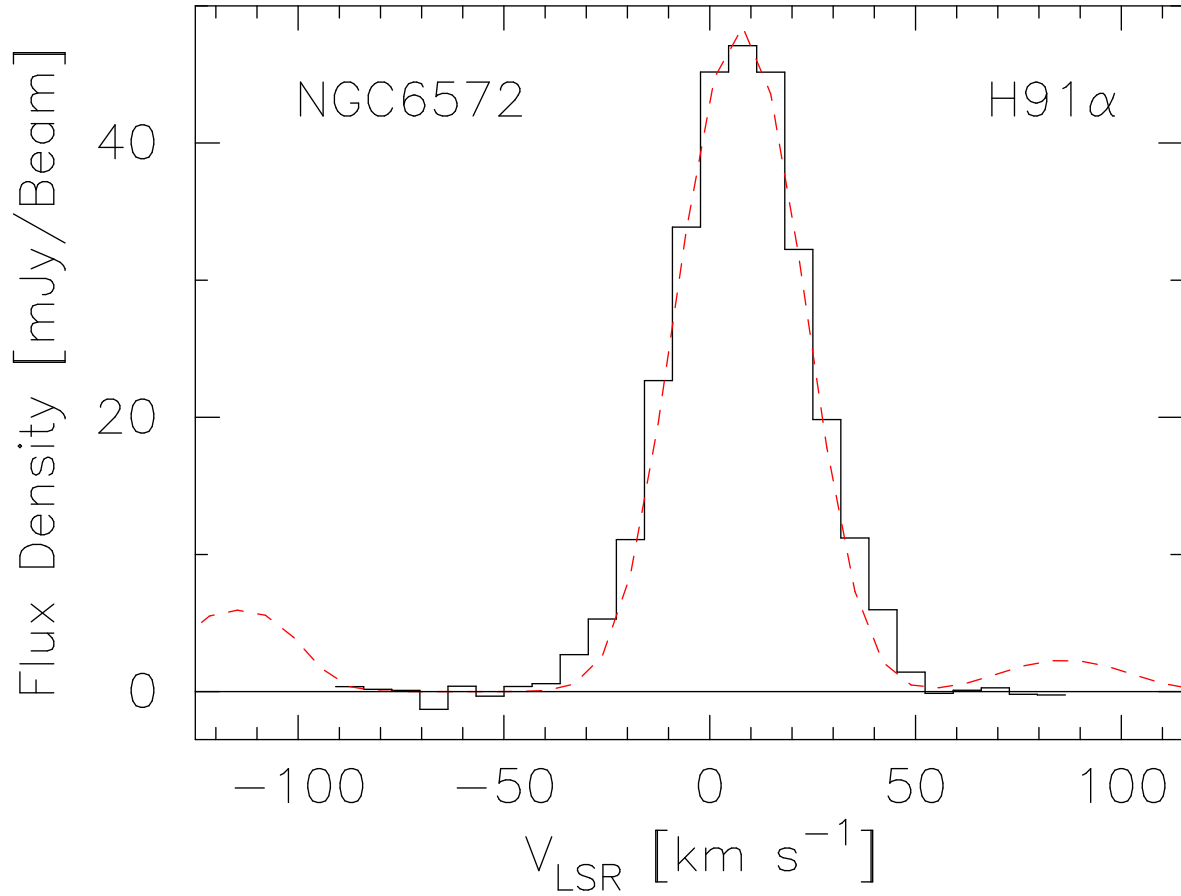


Fig. 4.— H91 $\alpha$  spectrum of NGC 6572. The solid histogram is the VLA data toward the peak continuum position. The dashed curve shows the NEBULA model assuming  $V_{\text{LSR}} = 8 \text{ km sec}^{-1}$ . The modeled line at negative velocities is the He91 $\alpha$  transition whereas the modeled line at positive velocities is the H 154 $\epsilon$  transition. The rms over the line-free spectral regions is  $500 \mu\text{Jy beam}^{-1}$ .

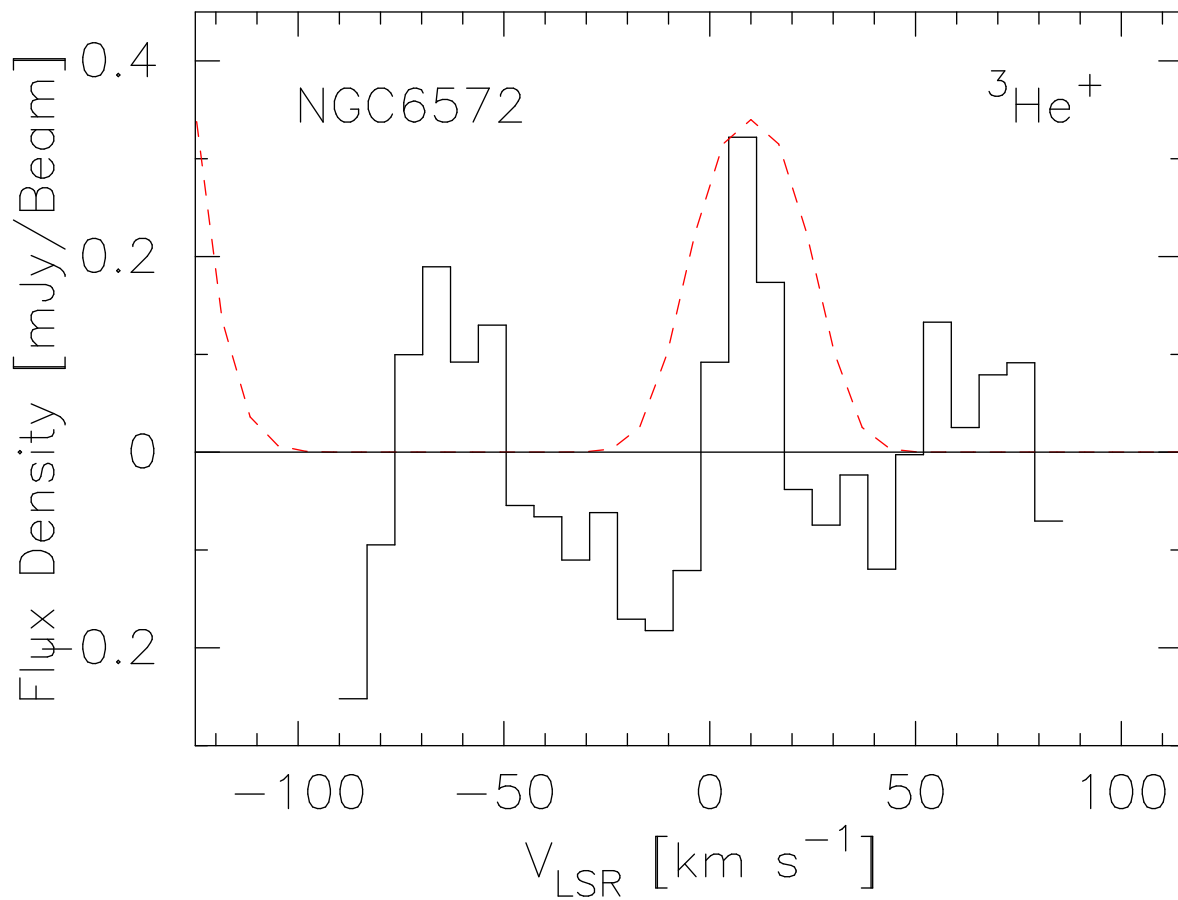


Fig. 5.—  ${}^3\text{He}^+$  spectrum of NGC6572. The solid histogram is the VLA data toward the peak continuum position. The dashed curve shows the NEBULA model assuming  $V_{\text{LSR}} = 8 \text{ km sec}^{-1}$ . The modeled line at negative velocity is the H 171 $\eta$  transition. The rms over the line-free spectral regions is  $100 \mu\text{Jy beam}^{-1}$ . The model  ${}^3\text{He}^+/\text{H}^+$  abundance ratio is  $1.0 \times 10^{-3}$  by number.

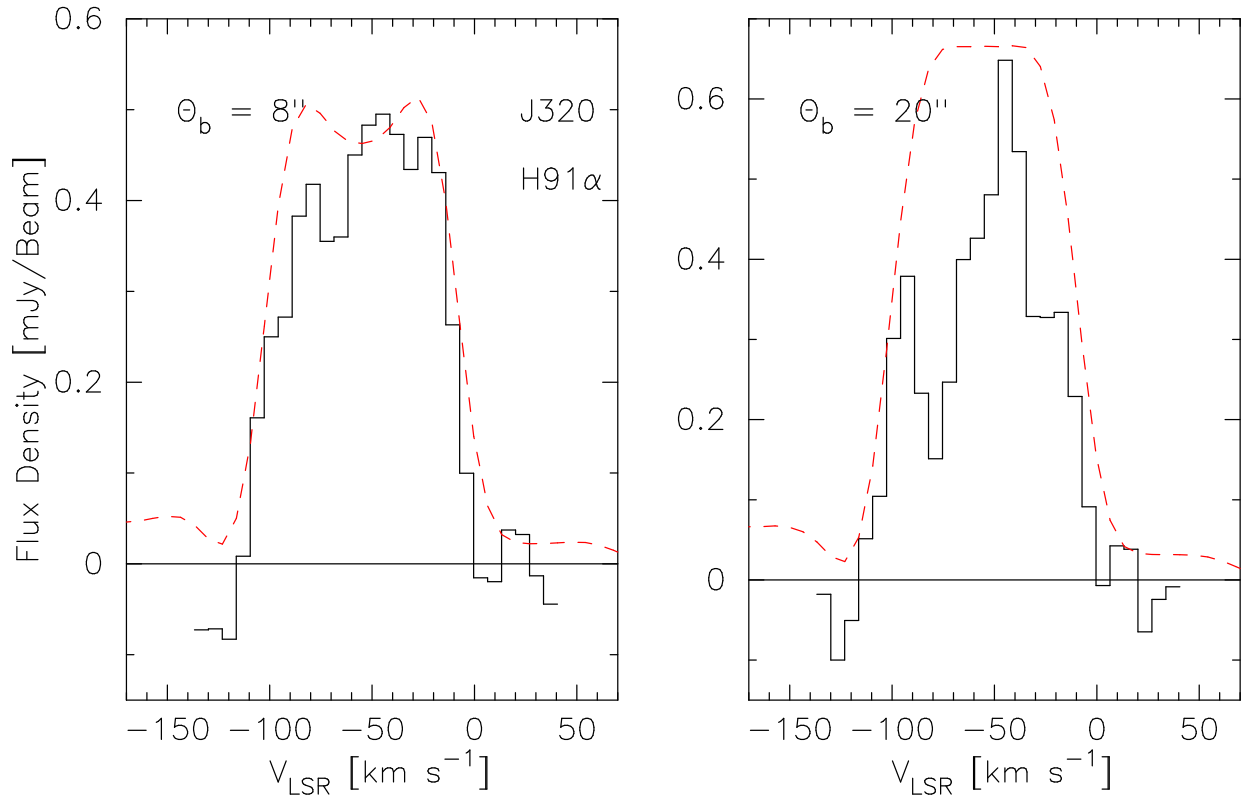


Fig. 6.— H91 $\alpha$  spectra of J320. The solid histograms are the VLA data and the dashed curves are the NEBULA model results assuming  $V_{\text{LSR}} = -54.9 \text{ km sec}^{-1}$ . Left panel: spectrum toward the peak continuum position for a synthesized HPBW of 8". The rms over the line-free spectral regions is  $50 \mu\text{Jy beam}^{-1}$ . Right panel: spectrum toward the peak continuum position for a synthesized HPBW of 20". The VLA image was convolved with a circular 20" beam using the task CONVL. The rms over the line-free spectral regions is  $70 \mu\text{Jy beam}^{-1}$ .

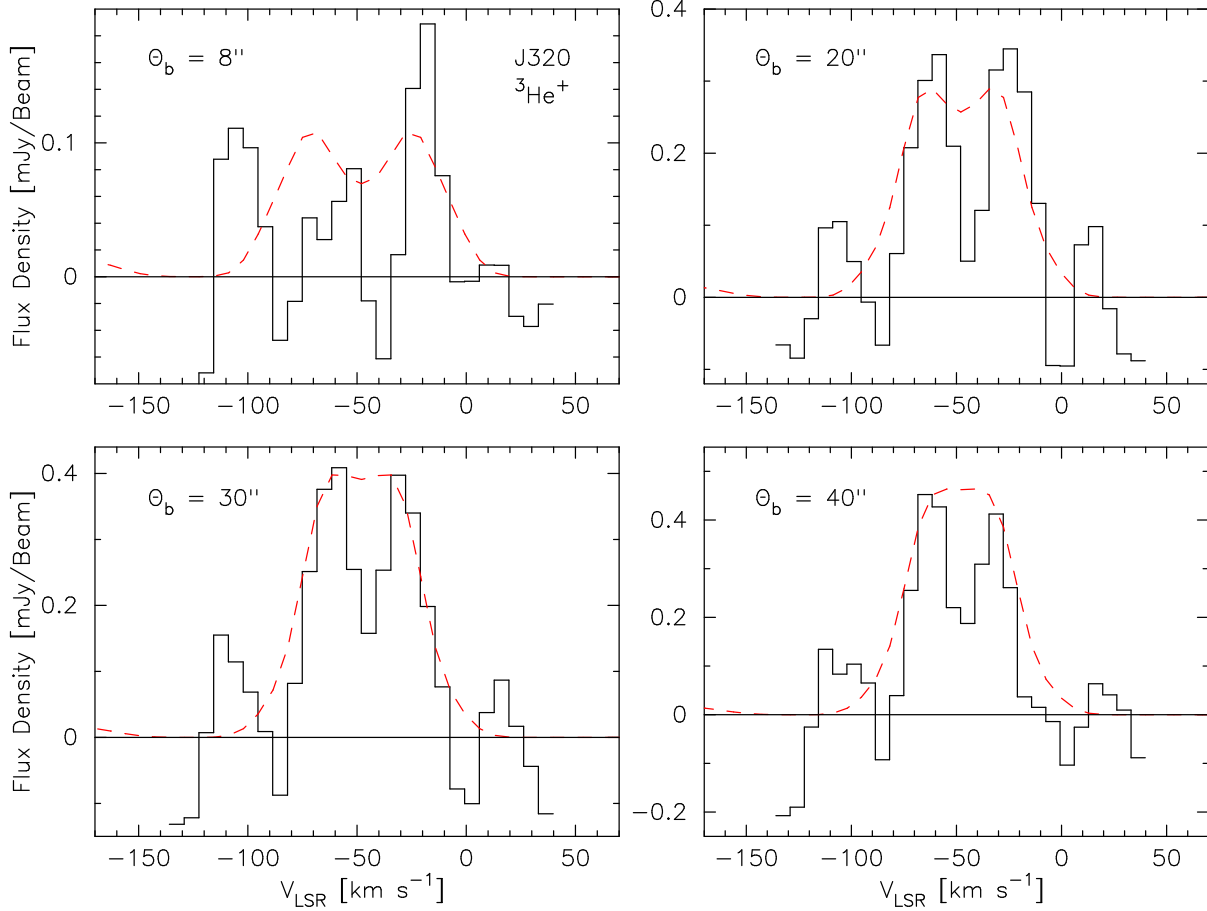


Fig. 7.—  ${}^3\text{He}^+$  spectra of J320. The solid histograms are the VLA data and the dashed curves are the NEBULA model results assuming  $V_{\text{LSR}} = -47.9 \text{ km sec}^{-1}$ . The VLA data were convolved with a circular beam using the task CONVL. The HPBW is shown in the top left corner of each panel. The rms values over the line-free spectral regions are 70, 110, 150, and  $190 \mu\text{Jy beam}^{-1}$  for HPBW's of 8, 20, 30, and  $40''$ , respectively. In the latter three cases the estimated  $S/N$  is 4. The model  ${}^3\text{He}^+/\text{H}^+$  abundance ratio is  $1.9 \times 10^{-3}$  by number.

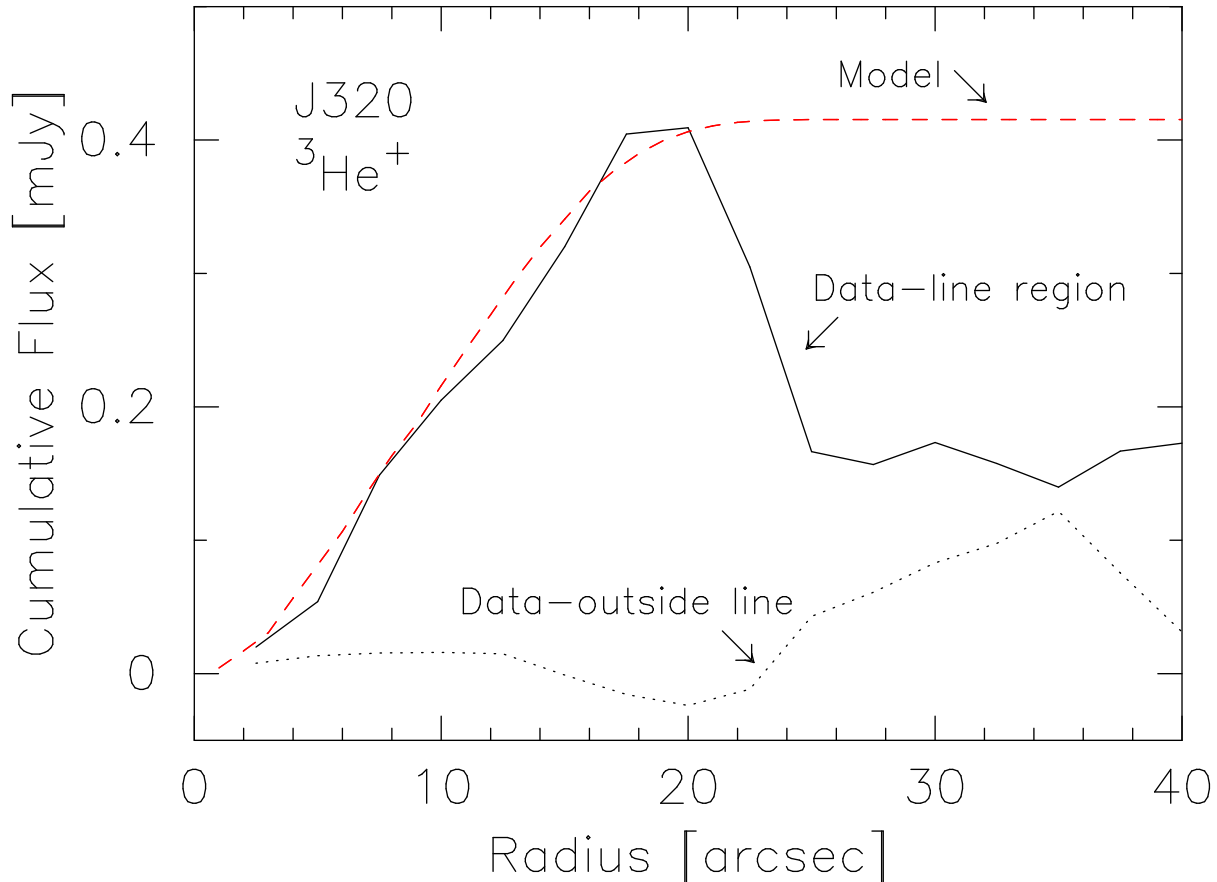


Fig. 8.— Cumulative  ${}^3\text{He}^+$  flux density versus radius for J320. The task IRING calculates the integrated flux density in concentric annuli from a specified center location. The solid curve is the cumulative flux density for the  ${}^3\text{He}^+$  image using the observed peak continuum emission as the center location. The cumulative flux at larger radii drops because of the missing short spacings. The dashed lines are the result of a similar analysis using the modeled data assuming a halo size of  $35''$  and an electron density of  $50\text{ cm}^{-3}$ . The model  ${}^3\text{He}^+/\text{H}^+$  abundance ratio is  $1.9 \times 10^{-3}$  by number. The missing short spacings do not affect the model. The dotted curve shows the result of a similar analysis made for  ${}^3\text{He}^+$  emission-free data channels. The rms of the cumulative flux in this noise image within a radius of  $20''$  is  $43\ \mu\text{Jy}$  whereas the peak cumulative  ${}^3\text{He}^+$  flux is  $400\ \mu\text{Jy}$  yielding a  $S/N$  for the line of  $\sim 9$ .

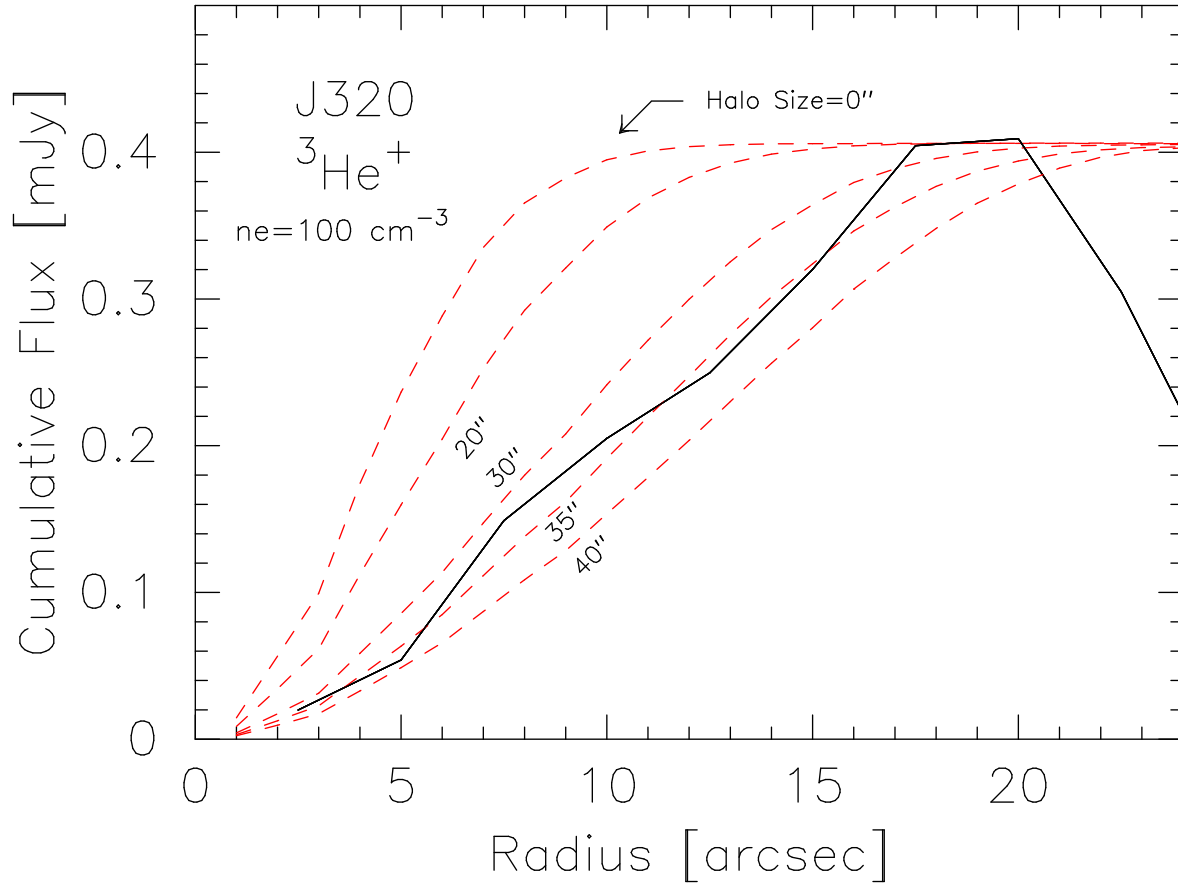


Fig. 9.— Cumulative  ${}^3\text{He}^+$  flux density versus radius for J320. The solid curve is that of Figure 8. The dashed lines are the results of a similar analysis using modeled data. The models have a halo electron density of  $100 \text{ cm}^{-3}$  and different halo sizes from left to right: 0, 20, 30, 35, and  $40''$ . The model results were scaled to match the peak  ${}^3\text{He}^+$  cumulative flux density.

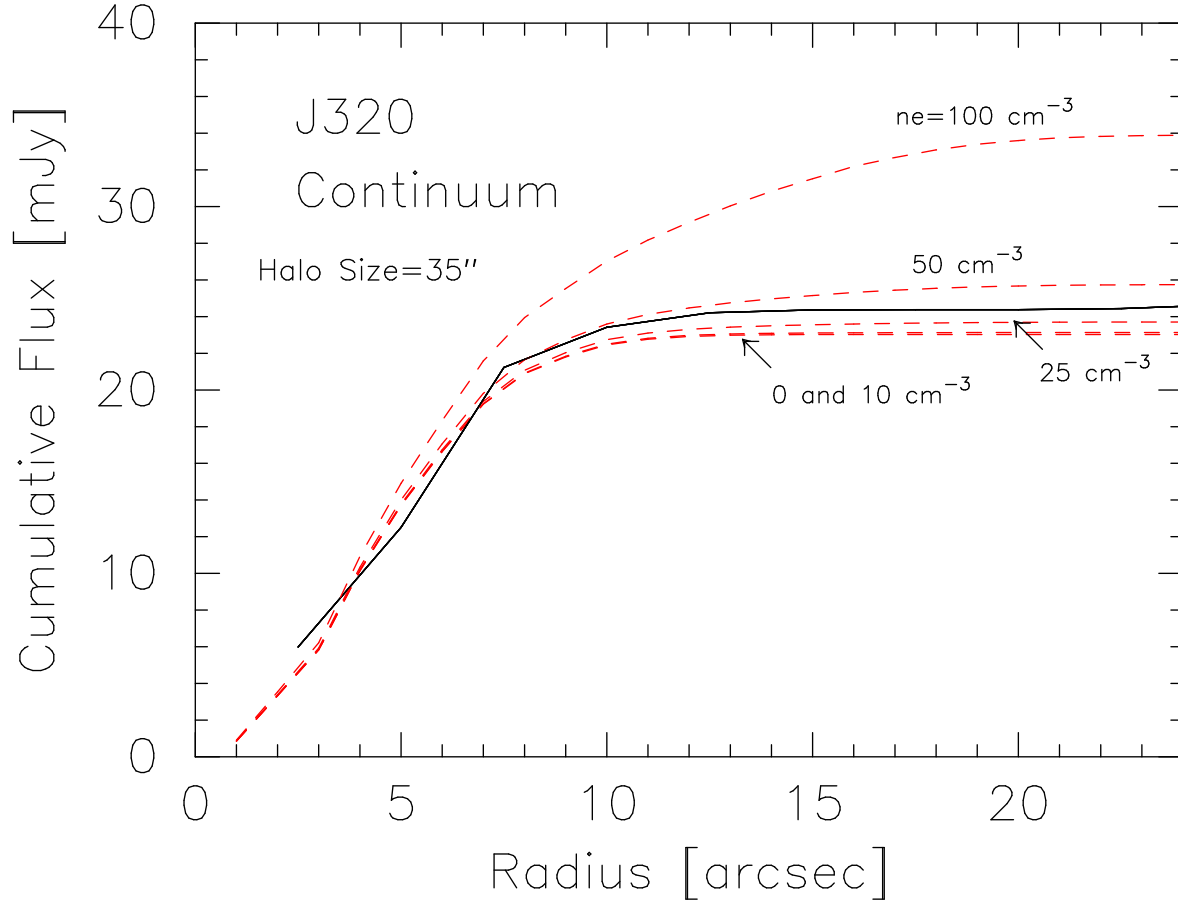


Fig. 10.— Cumulative continuum flux density versus radius for J320. The solid curve is the cumulative flux density for the continuum image using the observed peak continuum emission as the center location. The dashed lines show the result of a similar analysis using modeled data. The models have a halo size of 35'' and different halo electron densities from bottom to top: 0, 10, 25, 50, and 100 cm<sup>-3</sup>.



Table 1. VLA Observational Parameters

Parameters	NGC 6572	J 320
Date	1995 February	1996 August
Total Time (hr) <sup>a</sup>	24	23
Configuration	D	D
R.A. of field center (B1950)	18 <sup>h</sup> 09 <sup>m</sup> 40.57 <sup>s</sup>	05 <sup>h</sup> 02 <sup>m</sup> 48.6 <sup>s</sup>
Dec. of field center (B1950)	06° 50′ 25″.5	10° 38′ 25″.0
FWHM of primary beam	5′.4	5′.4
FWHM of synthesised beam	8″.20 × 7″.49	7″.82 × 7″.51
PA of beam	−14°	−2°
Total bandwidth (MHz)	6.25	6.25
Number of channels	31	31
LSR central velocity (km sec <sup>−1</sup> )	8.0	−37.9
Spectral resolution (kHz, km sec <sup>−1</sup> )	195.3 (6.8) <sup>b</sup>	326.2 (11.4) <sup>c</sup>
Flux density calibrator	B1328+307/B0134+329	B1328+307/B0134+329
Phase calibrator	B1730−130/B1749+096	B0446+112/B0316+413
Line channel <i>RMS</i> (μJy beam <sup>−1</sup> ) <sup>d</sup>	100	70
Continuum <i>RMS</i> (μJy beam <sup>−1</sup> ) <sup>d,e</sup>	280	90

<sup>a</sup>Approximate time not excluding edited data.

<sup>b</sup>On-line Hanning smoothed.

<sup>c</sup>Off-line Hanning smoothed.

<sup>d</sup>Using the <sup>3</sup>He<sup>+</sup> band.

<sup>e</sup>Dominated by dynamic range.

Table 2. VLA 8.7 GHz Continuum Properties<sup>a</sup>

Source	$\alpha$ (1950)			$\delta$ (1950)			Peak Flux Density (Jy beam <sup>-1</sup> )	Integrated Flux Density (Jy)	Angular Size FWHM (arcsec)
NGC 6572	18	09	40.54	06	50	25.4	0.97	1.25	8.4 × 9.4
J 320	05	02	48.35	10	38	21.0	0.018	0.024	8.3 × 9.4

<sup>a</sup>Based on two-dimensional Gaussian models.

Table 3. Planetary Nebula Model Parameters

Source	$\theta_{\text{inner}}$ (arcsec)	$\theta_{\text{outer}}$ (arcsec)	$V_{\text{exp}}$ (km sec <sup>-1</sup> )	$T_e$ (K)	$n_e$ (cm <sup>-3</sup> )10 <sup>3</sup>	( <sup>4</sup> He <sup>+</sup> /H <sup>+</sup> )	( <sup>4</sup> He <sup>++</sup> /H <sup>+</sup> )	( <sup>3</sup> He <sup>+</sup> /H <sup>+</sup> )10 <sup>3</sup>
NGC 6572	2.0	7.9	15.0	10300	22.0	0.11	0.00	1.0
J 320	2.0	7.4	46.0	7500	1.5	0.10	0.00	1.9
J 320 (halo)	7.4	35.0	25.0	7500	0.05	0.10	0.00	1.9